

# High-resolution spectroscopy of the variable hot post-AGB star LS 4331 (IRAS 17381-1616)

Natalia P. Ikonnikova<sup>1</sup>, Mudumba Parthasarathy<sup>2,\*</sup>, Ivan A. Shaposhnikov<sup>1,3</sup>, Svetlana Hubrig<sup>4</sup> and Geetanjali Sarkar<sup>5</sup>

<sup>1</sup> Lomonosov Moscow State University, Sternberg Astronomical Institute, 13 Universitetskij prospekt, Moscow 119234, Russia.

<sup>2</sup> Indian Institute of Astrophysics, Bangalore 560034, India.

<sup>3</sup> Lomonosov Moscow State University, Faculty of Physics, 1 Leninskie Gory, Moscow 119991, Russia.

<sup>4</sup> Leibniz Institute for Astrophysics (AIP), Potsdam, D-14482, Germany.

<sup>5</sup> Department of Physics, Indian Institute of Technology, Kanpur-208016, UP, India.

\*Corresponding author. E-mail: m-partha@hotmail.com

MS received 18 January 2024; accepted 18 January 2024

## Abstract.

An analysis of high-resolution ( $R \sim 48\,000$ ) optical spectrum of hot (B1Ibe) post-AGB star LS 4331 (IRAS 17381-1616) is presented. The detailed identification of the observed absorption and emission features in the wavelength range 3700–9200 Å is carried out for the first time. From non-LTE analysis of absorption lines the atmospheric parameters and chemical composition of the star are derived. We estimate  $T_{\text{eff}} = 20\,900 \pm 500$  K,  $\log g = 2.57 \pm 0.08$ ,  $V_r = -51.7 \pm 0.8$  km s<sup>-1</sup>,  $\xi_t = 24 \pm 4$  km s<sup>-1</sup> and  $v \sin i = 30 \pm 5$  km s<sup>-1</sup>. A abundance analysis for C, N, O, Mg, Al, S and Si reveals that the N and O abundance is close to solar while metal underabundances relative to the solar value (i.e. [Mg/H] = -1.04 dex, [Al/H] = -1.20 dex, [Si/H] = -0.46 dex) are found. We conclude that LS 4331 is a high galactic latitude metal-poor and carbon deficient hot post-AGB star. The underabundance of carbon ([C/H] = -0.64 dex) is similar to that found in other hot post-AGB stars and indicates that the star's AGB phase of evolution was terminated before the third dredge up. From the nebular emission lines the plasma diagnostics are derived. The presence of nebular emission lines in the spectrum of LS 4331 indicates that the photoionization of circumstellar envelope has already started. The nebular parameters and expansion velocity of the nebula is derived. Using the Gaia DR3 distance the absolute luminosity of the star is derived and the star's position on the post-AGB evolutionary tracks suggests that its initial main sequence mass is about  $1.2M_{\odot}$ . It is also reported that fast irregular brightness variations with an amplitude of up to 0.3 mag in V band have been found in the star, typical of hot post-AGB objects.

**Keywords.** post-AGB stars – atmospheres – abundance – early-type – evolution – IRAS 17381-1616.

## 1. INTRODUCTION

The late type (K, G, F) to hot (A, B, O) type post-AGB supergiants form an evolutionary sequence in the transition region from the tip of the AGB to early stages of planetary nebulae (Parthasarathy 1993, 1994). The time taken for hot post-AGB supergiants to evolve into a young planetary nebula is relatively very short and it is possible to study this rapid phase of evolution in real time in some cases. Analysis of high resolution spectra of only very few hot post-AGB stars has been carried out (Mooney *et al.* 2002, Klochkova *et al.* 2002, Sarkar *et al.*

2005, Mello *et al.* 2012, Ikonnikova *et al.* 2020 and references therein). Some of the hot post-AGB stars are high galactic latitudes and some are high velocity stars which suggests that their progenitor stars are of low mass. There are hot post-AGB stars in globular clusters. Therefore the study hot post-AGB stars enable us to further understand the advanced stages of post-AGB phase of evolution of low mass stars. Cool and hot post-AGB stars were found among high galactic latitude stars and high velocity stars (Parthasarathy & Pottasch 1986, 1989, Parthasarathy *et al.* 2020). Multi-wavelength studies of these stars, their circumstel-

lar shells and chemical compositions proved that they are indeed in the post-AGB stage of evolution. Only low and intermediate mass stars go through the post-AGB stage of evolution. Massive supergiants are not expected at high galactic latitudes. High galactic latitude supergiants were found to be in post-AGB stage of evolution (Parthasarathy & Pottasch 1986). Low-mass stars during their post-AGB phase of evolution mimic the spectra of supergiants. Because they have thin extended atmospheres around the CO core. Same is true with the high velocity post-AGB stars. Chemical composition of some of the high velocity supergiants and their IRAS flux distributions indicated that they are in post-AGB stage of evolution (for example, V886 Her, LS IV -12 111, LS II +34 26 etc). Hence the progenitors of these high galactic latitude and high velocity post-AGB stars are low-mass stars.

In order to further understand this rapid phase of evolution, chemical composition patterns, onset of the photoionization of the shell, and late thermal pulse (LTP) objects it is important to study many hot post-AGB stars. This is an effort in that direction.

The star LS 4331 (Sp Type=OB+, Pmag=12.2 mag) from the Catalog of Luminous stars in the Southern Milky Way by Stephenson & Sanduleak (1971) was found to be an infrared (IR) source IRAS 17381-1616 with far-IR (IRAS) colours and far-IR flux distribution similar to that of planetary nebulae and post-AGB stars and hence it was classified as a high galactic latitude ( $b = +7.5^\circ$ ) hot post-AGB star (Parthasarathy *et al.* 2000). From a low resolution spectrum of this star (Parthasarathy *et al.* 2000) found the spectral-type to be B1Ibe. Its IRAS colours and IRAS flux distribution and characteristics of the circumstellar dust shell and spectral type are similar to that of post-AGB B-supergiant LS II +34 26 (Parthasarathy 1993, 1994; García-Lario *et al.* 1997). Suárez *et al.* (2006) classified the object as a planetary nebula. Cerrigone *et al.* (2011) and references therein detected the radio continuum indicating that it is in the very young planetary nebula stage. Cerrigone *et al.* (2009) observed this star with the Spitzer space telescope and detected silicate feature in the IR indicating that the circumstellar envelope is Oxygen-rich. Some parameters of LS 4331 are summarized in Table 1.

We have been carrying out detailed analysis of ESO FEROS high resolution spectra of hot post-AGB stars and young planetary nebulae (Otsuka *et al.* 2017, Arkhipova *et al.* 2018, Ikonnikova *et al.* 2020, Herrero *et al.* 2020). There is no detailed

study of the spectrum of LS 4331. In this paper we present a detailed analysis of the high resolution spectrum of LS 4331 in order to identify emission and absorption lines, and to understand its chemical composition and evolutionary stage. In addition, we have studied the photometrical behavior of the star and have discovered its rapid variability in brightness.

The paper is organized as follows: in Sect. 2 we describe the observations and the data reduction; in Sect. 3 we present an analysis of the main spectral features; the estimation of atmospheric parameters and abundances are presented in Sect. 4. In Sect. 5 we analyze the emission spectrum. Photometric observations and their analysis are presented in Sect. 6. The evolutionary status of the star is discussed in Sect. 7. In Sect. 8 we discuss the results and in the last section we summarize our conclusions.

## 2. Observations and data reduction

### 2.1 High resolution spectroscopy

The high-resolution optical spectrum of LS 4331 was obtained on April 16, 2006 (MJD=53841.255) with the Fiberfed Extended Range Optical Spectrograph (FEROS; Kaufer *et al.* 1999) on the 2.2-meter ESO/MPG telescope at La Silla Observatory, Chile (Proposal ID.77.D-0478A, PI: M. Parthasarathy). Observations of this star were carried out along with other hot post-AGB stars to determine their chemical composition (see Otsuka *et al.* 2017, Arkhipova *et al.* 2018, Ikonnikova *et al.* 2020, Herrero *et al.* 2020). The FEROS spectra have a resolution of  $R \sim 48000$  and a wavelength range from 3600 to 9200 Å in 39 orders. The CCD detector EEV 2k×4k with 15 μm pixel size was used. The exposure time for each spectrum was 2700 s. The signal-to-noise ratio was 100 per pixel at 5500 Å.

The reduction process was performed using the FEROS standard online reduction pipeline and the echelle spectra reduction package ECHELLE in IRAF using a standard reduction manner including bias subtraction, removing scattered light, detector sensitivity correction, removing cosmic ray hits, airmass extinction correction, flux density calibration, and an all echelle order connection. Both reduced spectra were continuum normalized, co-added, and cleaned of telluric lines with MOLECFIT (Kausch *et al.* 2015).

**Table 1.** Stellar and dust parameters of LS 4331 from the literature.

Quantity	Value	References
Position (J2000.0)	$\alpha = 17^{\text{h}}41^{\text{m}}00^{\text{s}}, \delta = -16^{\circ}18'12''$ (2000)	SIMBAD
Gal. coord	$l = 010.255, b = +07.493$	SIMBAD
Proper motions (mas/yr)	$\mu_{\alpha} = -0.167 \pm 0.024, \mu_{\delta} = -9.421 \pm 0.015$	G21
Parallaxes (mas)	$0.1086 \pm 0.0249$	G21
Distance (pc)	8256 (7439–9305)	BJ21
Spectral type	OB+, B1Ibe	SS71, P00
$T_{\text{eff}}$ (K)	24000	C09
Magnitude	13.57( <i>B</i> ) 13.22( <i>V</i> ) 13.22( <i>R</i> )	UCAC4
	13.36( <i>g</i> ) 13.07( <i>r</i> ) 13.11( <i>i</i> )	UCAC4
	12.306( <i>J</i> ) 12.157( <i>H</i> ) 12.046( <i>K<sub>S</sub></i> )	2MASS
	13.084( <i>G</i> ) 13.251( <i>BP</i> ) 12.685( <i>RP</i> )	G21
$T_{\text{dust}}$ (K)	250, 120	C09

References. SIMBAD: <http://simbad.u-strasbg.fr/simbad/>; SS71: Stephenson & Sanduleak (1971); P00: Parthasarathy *et al.* (2000); C09: Cerrigone *et al.* (2009); UCAC4: Zachariah *et al.* (2013); G21: Gaia Collaboration *et al.* (2021); BJ21: Bailer-Jones *et al.* (2021)

## 2.2 Photometric data

**2.2.1 Multicolour photometry.** Optical photometry for the star was obtained on the 60-cm Ritchey-Crétien telescope (RC600) at the Caucasian mountain observatory (CMO) of Moscow State University. The telescope is equipped with a set of photometric filters and an Andor iKon-L CCD (2048×2048 pixels of 13.5  $\mu\text{m}$ , the pixel scale is 0''.67 pixel<sup>-1</sup>, the field of view is 22' × 22'). For a more detailed description of the telescope and instrumentation we refer to Berdnikov *et al.* (2020). We have observed LS 4331 for three seasons of visibility in 2021–2023. A complete set of exposures for each night consisted of 2–3 frames in each of the *BVR<sub>C</sub>I<sub>C</sub>* and *gri* filters. The observations and data reduction (correction for bias, dark, and flat fields) were performed using the MaxIm DL6 program<sup>1</sup>. Aperture photometry for each system was performed with the AstroImageJ software package (Collins *et al.* 2017) using the comparison stars noted in Table 2. The comparison stars' magnitudes were adopted from Synthetic photometry generated from the Gaia BP/RP mean spectra<sup>2</sup>. Fig. 1 provides a finding chart for LS 4331 and comparison stars.

We present the resulting photometry for LS 4331 in Appendix A. where for every night we list the mean time of observation and magnitudes in each of photometric bands averaged over 2–3

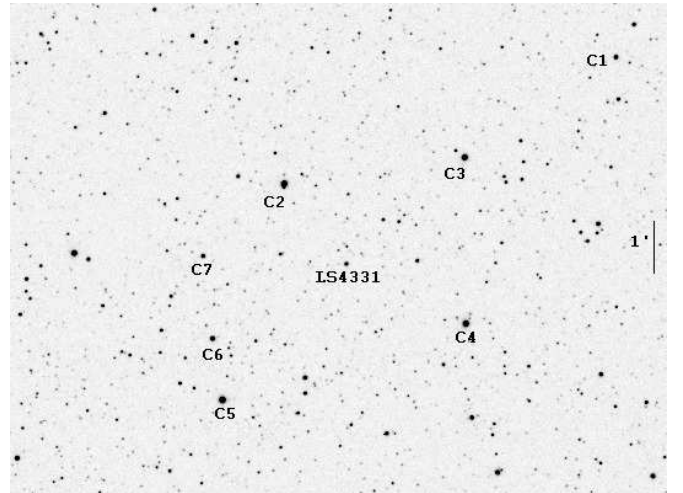


**Figure 1.** Finding chart for the field of LS 4331 in *R<sub>C</sub>*. The abbreviations C1...C7 refer to the comparison stars mentioned in Table 2.

<sup>1</sup><https://maxim-dl.software.informer.com/6.0/>

<sup>2</sup><https://vizier.cds.unistra.fr/viz-bin/VizieR-3?-source=I/360/syntphot>

**Table 2.** Comparison stars

Star	<i>B</i>	<i>V</i>	<i>R<sub>C</sub></i>	<i>I<sub>C</sub></i>	<i>g</i>	<i>r</i>	<i>i</i>
C1	13.114±0.015	12.555±0.008	12.206±0.006	11.848±0.005	12.770±0.010	12.388±0.007	12.250±0.005
C2	10.833±0.026	10.595±0.011	10.430±0.006	10.232±0.006	10.615±0.019	10.572±0.008	10.597±0.006
C3	11.513±0.025	11.041±0.010	10.742±0.008	10.432±0.008	11.200±0.014	10.913±0.009	10.822±0.008
C4	12.526±0.026	11.134±0.011	10.391±0.007	9.724±0.006	11.835±0.019	10.659±0.008	10.211±0.006
C5	12.070±0.022	10.844±0.010	10.174±0.006	9.550±0.005	11.442±0.016	10.429±0.007	10.024±0.006
C6	14.790±0.053	12.854±0.014	11.693±0.006	10.532±0.006	13.905±0.032	12.133±0.009	11.150±0.006
C7	14.625±0.027	13.278±0.012	12.518±0.007	11.797±0.006	13.961±0.019	12.803±0.008	12.297±0.006

frames. Our uncertainties defined as standard deviations for each night and averaged over all nights are  $\Delta B = 0.029$  mag,  $\Delta V = 0.013$  mag,  $\Delta R_C = 0.009$  mag,  $\Delta I_C = 0.014$  mag,  $\Delta g = 0.021$  mag,  $\Delta r = 0.010$  mag and  $\Delta i = 0.009$  mag.

**2.2.2 ASAS-SN data.** To study the nature of the variability of the star, we also investigated the much more numerous and wide-ranging observations from All Sky Automated Survey for Supernovae (ASAS-SN, Shappee *et al.* 2014; Kochanek *et al.* 2017). The survey uses several cameras on five different good astronomical sites to acquire its data. The field of view of each camera is roughly  $4.5 \text{ deg}^2$ , the pixel scale is  $8.''0$ , and the image FWHM is  $\sim 2$  pixels (Kochanek *et al.* 2017). The data are available for download through the ASAS-SN web page<sup>3</sup>. Observations were conducted using several small telescopes in two photometrical bands: with a *V* filter from the beginning of 2015 to the middle of 2018, and with a *g* filter from the beginning of 2018 until now. ASAS-SN *V*-band data of LS 4331 span a time interval from February 16, 2015 to September 23, 2018. ASAS-SN *g*-band data (using the Sloan Digital Sky Survey (SDSS) *g* filter) for LS 4331 became available from April 20, 2018 and continue until to October 22, 2023. We utilized images of good quality, excluding those taken in poor weather with  $\text{FWHM} > 2$  pixels. We also removed data with a large standard deviation ( $> 0.03$  mag). Finally, we were left with 591 data points in the *V* band and 2232 in the *g* band for analysis.

### 3. Description of the high-resolution spectrum

The optical spectrum of LS 4331 shows stellar absorption lines, nebula emission lines, and interstel-

lar absorption features. Lines identification are based on the National Institute of Standards and Technology (NIST) Atomic Spectra Database<sup>4</sup>. The detailed spectral atlas, which lists the observed and synthetic spectrum of LS 4331, is presented at <sup>5</sup>. Absorption features with the equivalent width (EW) of more than  $35 \text{ m\AA}$  are marked in black, identified emission lines are marked in red, and features of the spectrum of interstellar origin are marked in blue. The Fig. 2 shows a fragment of the spectrum from the atlas.

#### 3.1 Photospheric absorption lines

Absorption lines of neutral species including H I, He I, and also singly ionized species including N II, O II, S II, C II and Mg II were detected. Higher ionization is seen in Al III, Si III, S III, C III and Si IV.

#### 3.2 Nebular emission lines

The list of emission lines in LS 4331 is given in Appendix B. It includes the measured and laboratory wavelength (in air), equivalent width (EW), the heliocentric radial velocity, the name of the element and the multiplet number to which the measured line belongs.

The hydrogen Balmer and Paschen lines consist of the broad photospheric absorption and nebular emission components. The emission components of hydrogen lines do not show a P Cyg profile. The H $\alpha$  and H $\beta$  lines are fully filled in by emission (Fig. 3).

The helium lines are not included in Appendix B. as they have complicated multi-component profiles due to the emission lines superposed on the corresponding absorption components. Fig. 4 shows the profiles of selected He I lines and compared to model spectra (see next). The emission lines are shifted to the left of

<sup>3</sup><https://asas-sn.osu.edu/>

<sup>4</sup><https://www.nist.gov/pml/atomic-spectra-database>

<sup>5</sup><https://www.sai.msu.ru/research/2024/atlas-LS4331.pdf>

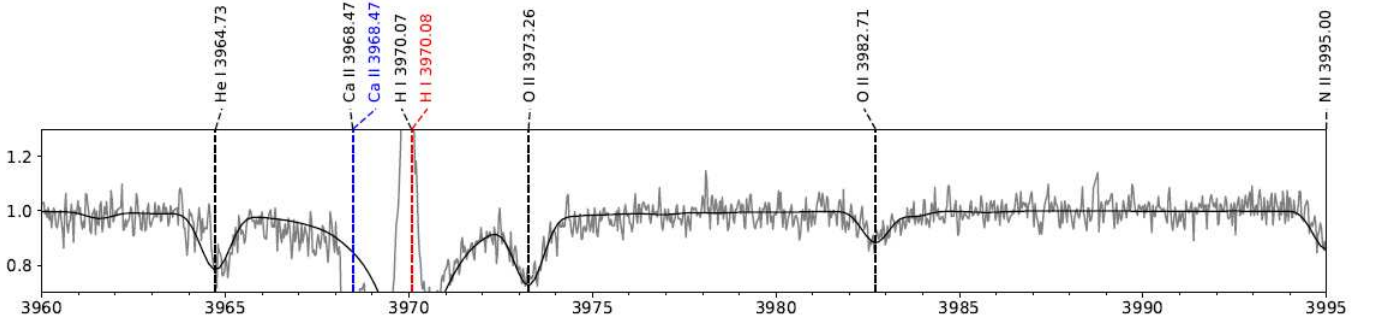


**Figure 2.** A fragment of the spectrum from the atlas.

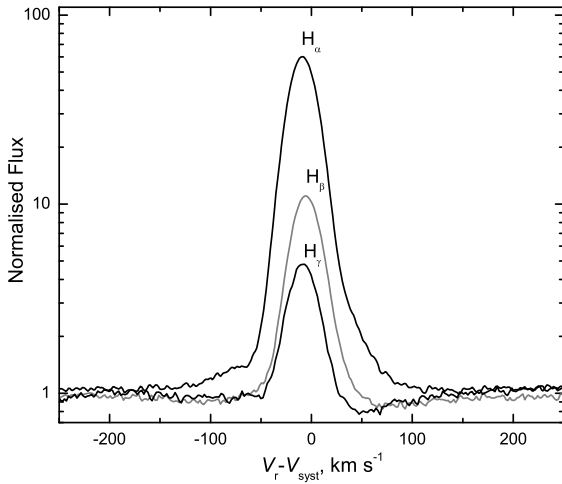


**Figure 3.** Profiles of  $H\alpha$ ,  $H\beta$  and  $H\gamma$  lines seen in the spectrum of LS 4331 on a velocity scale relative to  $V_{\text{sys}} = -52 \text{ km s}^{-1}$ .

the absorption lines, accordingly, they have lower radial velocities.

The permitted emission lines, in addition to hydrogen and helium, belong to the ions of SiII, CII, MgII, FeIII and also to the nonionised atoms of OI and NI. In the red spectral region, the permitted OI  $\lambda 8446$  triplet is the most remarkable emission feature. The forbidden emission lines are from [FeII], [NiII]  $\lambda 7378, 7412$ , [NII]  $\lambda 5755, 6548, 6584$ , [SII]  $\lambda 6717, 6731$ , [CrII], [OI]  $\lambda 5577, 6300, 6363$  as well as and [SIII]  $\lambda 9069$ .

### 3.3 Interstellar features

The spectrum of LS 4331 contains absorption features that have interstellar origin. There are NaI doublet ( $\lambda 5889.951, 5895.924$ ), CaII H and K lines

( $\lambda 3968.469, 3933.663$ ) and KI lines ( $\lambda 7664.899, 7698.974$ ). The H line of CaII is very much blended with the strong stellar  $H\epsilon$  line. The selected interstellar spectral lines are depicted in the right panel of Fig. 5. The KI lines show a single and sharp profiles with the radial velocities of  $-7.8 \pm 0.3 \text{ km s}^{-1}$  and  $-55.2 \pm 0.2 \text{ km s}^{-1}$ . The NaI and CaII lines have broad multi-component profiles. The main broad component contains details that correspond to velocities of  $0.5 \text{ km s}^{-1}$  and  $-8.0 \text{ km s}^{-1}$ . The average velocity of the other broad component is  $V_r \approx -55 \text{ km s}^{-1}$  agrees with that of the short-wavelength component of the KI line. As we have determined, the radial velocity of the star is  $-51.7 \pm 0.8 \text{ km s}^{-1}$  (see Subsection 4.1), while the average velocity obtained from emission lines of the circumstellar envelope corresponds to  $-60.3 \pm 4.7 \text{ km s}^{-1}$  (see Subsection 5.2). Therefore, it can be deduced that the KI, CaII and NaI absorption lines with velocities of circa  $-55 \text{ km s}^{-1}$  are formed in the expanding envelope around the central star.

In addition to the above-mentioned interstellar atomic lines, our echelle spectra contain several quite strong diffuse interstellar bands (DIBs):  $\lambda 5781.48, 5798.06, 5850.81, 5889.95, 5895.92, 6196.98, 6204.05, 6285.04, 6380.62, 6614.82, 6994.13, 7116.31, 7120.71, \text{ and } 7225.53$ , where the central wavelengths are identified in accordance with Hobbs *et al.* (2008). The profiles of several DIBs are shown in the left panel of Fig. 4. The average heliocentric velocity  $V_r$  derived from the DIBs interstellar absorption bands agrees with the velocity of the NaI and CaII main components:  $V_r \approx -8.0 \text{ km s}^{-1}$ .

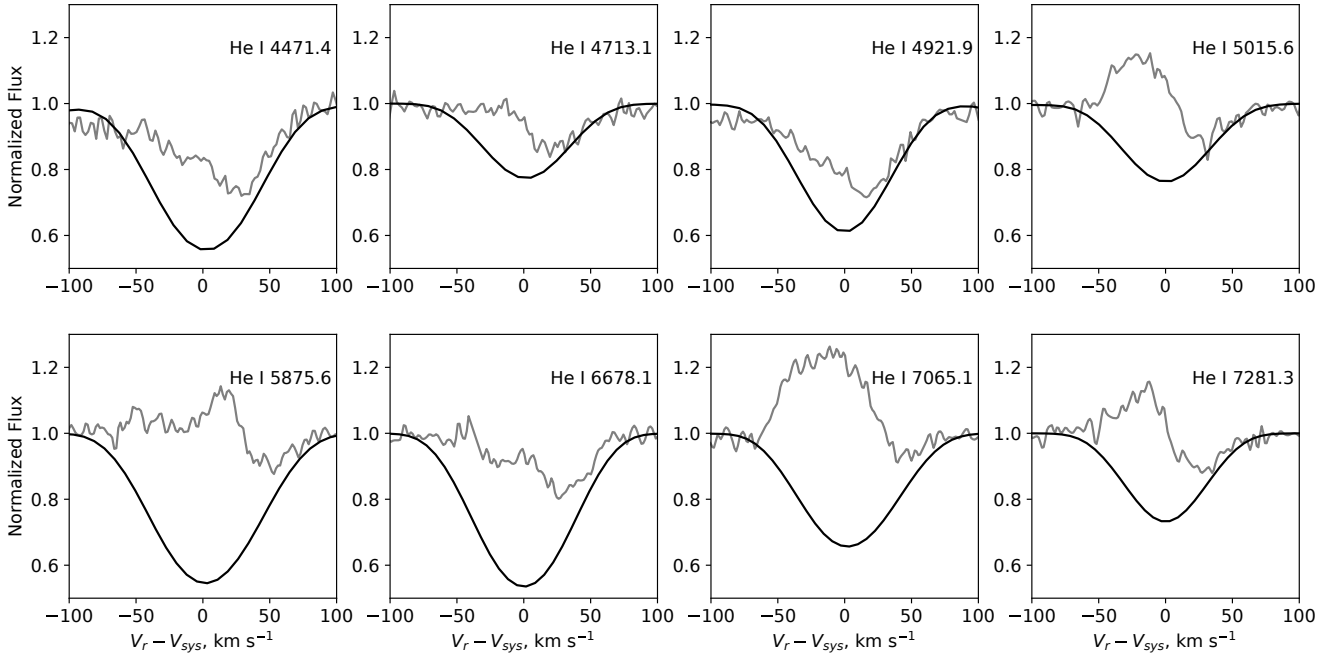


**Figure 4.** The profiles of selected He I lines seen in the spectrum of LS 4331 on a velocity scale relative to  $V_{sys} = -52$  km s<sup>-1</sup> and compared to model spectra.

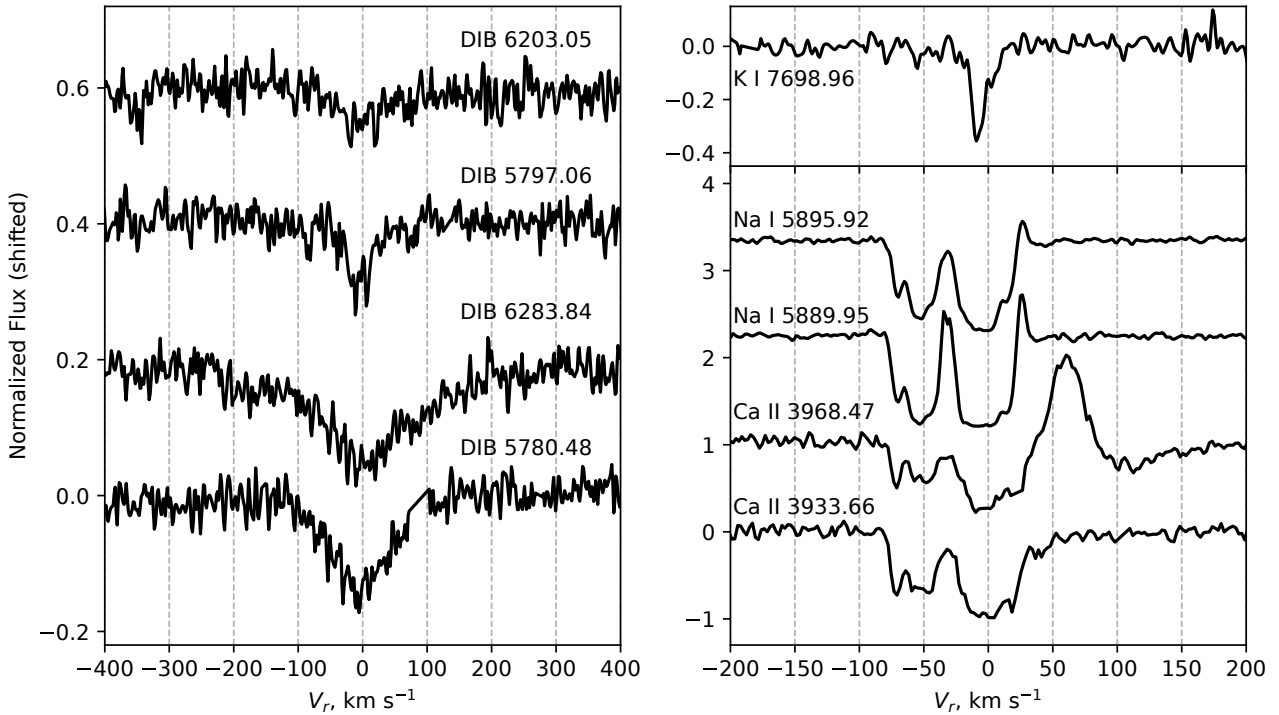


**Figure 5.** The profiles of interstellar absorption lines of Ca II, Na I, and KI (the right panel) and four strongest DIBs (the left panel) in the spectrum of LS4331.

#### 4. Determination of the atmospheric parameters

The stellar parameters ( $T_{\text{eff}}$ ,  $\log g$ ,  $v \sin i$ ,  $\xi_t$ ,  $v \sin i$ ) and elemental abundances are determined by fitting synthetic line profiles to the observed ones. The synthetic profiles were calculated with SYN-SPEC v.49 available at <sup>6</sup>, using the BSTAR2006 grids generated with the code TLUSTY (Hubeny & Lanz 1995), which assumes a plane-parallel atmosphere in radiative, statistical non-local thermodynamic equilibrium (non-LTE).

In cases where line profiles are distorted, for example by the presence of emission components in the blue wing, the observed profile was approximated by a synthetic profile through minimization of  $\chi^2$ . Poor or distorted parts of the profile were ignored.

The element abundance obtained from individual lines are averaged with weights according to their uncertainties. Certain parameters are inter-related, so by iteratively we derive a self-consistent set of parameters.

##### 4.1 Radial velocity

We selected 25 absorption lines, shapes of which are well fitted by theoretical ones. We did not include lines with emission features or with noticeably asymmetrical profiles. The wavelengths shifts were found by fitting Gaussian profiles to both observed and synthetic spectra in the same wavelength range. Average measurements for each ion are presented in Appendix C. The weighted average value along all lines gives the heliocentric velocity of the star  $V_r = -51.7 \pm 0.8 \text{ km s}^{-1}$ .

##### 4.2 Surface gravity $\log g$ and effective temperature $T_{\text{eff}}$

Surface gravity  $\log g$  and effective temperature,  $T_{\text{eff}}$ , were determined from the wings of hydrogen lines and from the balance of ionization states of silicon (SiIII/SiIV). The H $\alpha$  and H $\beta$  lines are filled in by emission components (see Fig. 3), so we used H $\gamma$ , H $\delta$ , H $\epsilon$  and H6 (see Fig. 6). By fitting the wings of the hydrogen lines under different assumptions about the temperature of the star, a sequence of  $T_{\text{eff}}-\log g$  pairs is obtained, which can be described by the equation  $\log g = -1.01 \pm 0.38 + (2.65 \pm 0.41) \cdot 10^{-4} \cdot T_{\text{eff}} - (4.5 \pm 1.0) \cdot 10^{-9} \cdot T_{\text{eff}}^2$  (Fig. 7). For these pairs of  $\log g$  and  $T_{\text{eff}}$ , we select silicon lines and adjust the  $\epsilon(\text{Si})$  content for each individual line to find the best fit. To do this,

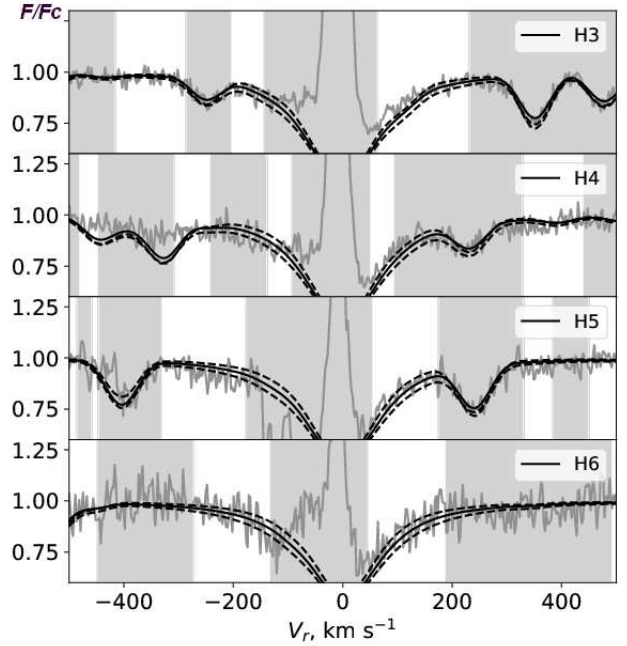


**Figure 6.** Wings of hydrogen lines. The shaded areas are ignored during the fit. The solid lines are for the best-fitting values of  $\log g$ .

we selected only non-blended lines: SiIII  $\lambda\lambda 4567.8$ ,  $4574.8$ ,  $5739.7$ , and SiIV  $\lambda 4116.1$ . From Fig. 8, it is clear that the abundances measured from SiIII and SiIV lines are in agreement with each other at  $T_{\text{eff}} = 20900 \pm 500 \text{ K}$  and  $\log g = 2.57 \pm 0.08$  and equal to  $\log \epsilon(\text{Si}) = 7.04 \pm 0.03$ .

##### 4.3 Microturbulence velocity

The microturbulence velocity,  $\xi_t$ , was derived from the analysis of 23 non-blended OII lines. For each line, we adjust oxygen abundance  $\epsilon(\text{O})$  for wide range of trial values  $\xi_t$ . The obtained dependencies of  $\epsilon(\text{O})$  on EW of the lines are shown in Fig. 9. The top panel shows the dependence of the slope  $\partial(\log \epsilon(\text{O}))/\partial(\text{EW})$  on the estimated microturbulence velocity, the bottom panel shows a detailed "EW -  $\epsilon(\text{O})$ " diagram for three values of  $\xi_t = 20, 24, 28 \text{ km s}^{-1}$ . These slope dependencies were calculated using the method of least squares, weighted by error. Based on these data, we estimate the microturbulence velocity as  $\xi_t = 24 \pm 4 \text{ km s}^{-1}$ . The weighted mean of  $\log \epsilon(\text{O}) = 8.57$  with a standard error of 0.02 dex and a standard deviation of 0.08 dex.

<sup>6</sup><http://tlusty.oca.eu/Synspec49/synspec-frames-down.html>



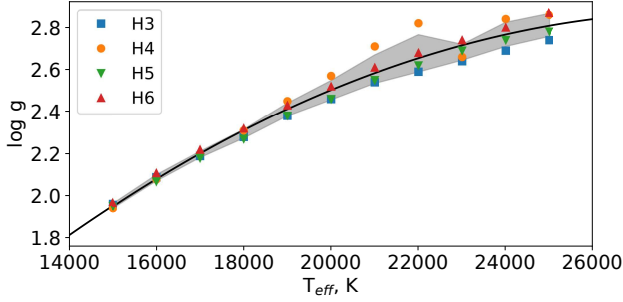


**Figure 7.** Parameters sequence estimated from hydrogen wings. Mean and sigma values were calculated for four lines at each point. The area between "mean-sigma" and "mean+sigma" is filled in gray.

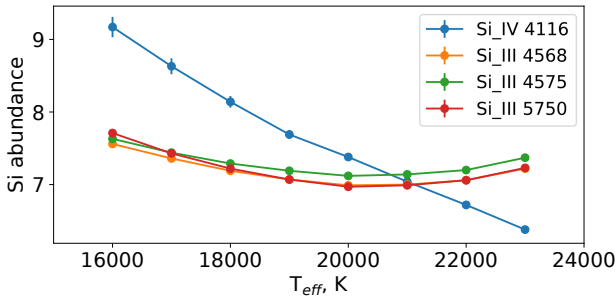


**Figure 8.** The silicon ionization balance.

**Table 3.** Element abundances determined for LS 4331 in  $\log \varepsilon = 12 + \log(n_X/n_H)$  and  $[X/H] = \log(n_X/n_H) - \log(n_{X\odot}/n_{H\odot})$

	$\log \varepsilon_{\odot}$	$\log \varepsilon$	$[X/H]$	$\sigma_x$	$\sigma_{\bar{x}}$	N
C	8.43	7.79	-0.64	0.14	0.10	2
N	7.83	7.45	-0.38	0.30	0.12	6
O	8.69	8.57	-0.12	0.08	0.02	23
Mg	7.60	6.56	-1.04	–	0.04	1
Al	6.45	5.25	-1.20	–	0.05	1
Si	7.51	7.04	-0.46	0.07	0.03	4
S	7.12	6.31	-0.81	0.06	0.05	2

Solar values  $\log \varepsilon_{\odot}$  are taken from Asplund *et al.* (2009).  $\sigma_x$  and  $\sigma_{\bar{x}}$  are the standard deviation and the standard error of mean for  $\log \varepsilon$ .

#### 4.4 Chemical abundances

The elemental abundances were determined for the following parameter set:  $T_{\text{eff}} = 20900$  K,  $\log g = 2.57$ , and  $\xi_t = 24$  km s<sup>-1</sup>. The non-LTE chemical abundances of 7 elements were obtained by matching the observed spectra with theoretical profiles generated with the Synplot code. The results for C, N, O, Mg, Al, Si and S were compiled into Table 3 along with their uncertainties. Fig. 10 shows the observed and theoretical profiles of some selected lines. We do not report the helium abundance in Table 3 as the obtained value of  $\log \varepsilon(\text{He}) = 10.61$  is unrealistic. The result is due to the fact that helium lines have distorted profiles due to the influence of emission components, which is visible on Fig. 4. Unfortunately, Ne and Fe lines in the spectrum LS 4331 are absent or too weak to calculate the abundance. Absorption lines used for measurement of the elemental abundances presented in Appendix C.

Determining the carbon abundance in LS 4331 is very difficult due to the fact that CII lines, which are most commonly used for this purpose ( $\lambda\lambda 3921, 4227, \text{ and } 4267$ ), are extremely weak. The CII lines at  $5120\text{--}5152$  Å and  $6780\text{--}6800$  Å, which were used by Mello *et al.* (2012) to determine the carbon abundance of a sample of hot post-AGB stars with parameters similar to LS4331, are absent in the spectrum of LS4331 and cannot be used by us. Fig. 11 shows observed profiles of some CII and CIII lines and synthetic ones for various  $\log \varepsilon(C)$ . The CII line  $\lambda 3921$  from the doublet  $\lambda\lambda 3919, 3921$  is practically not visible. Fitting the profile of the  $\lambda 3719$  line gives an abundance of  $7.25 \pm 0.25$ ; the abundance obtained from the EW measured



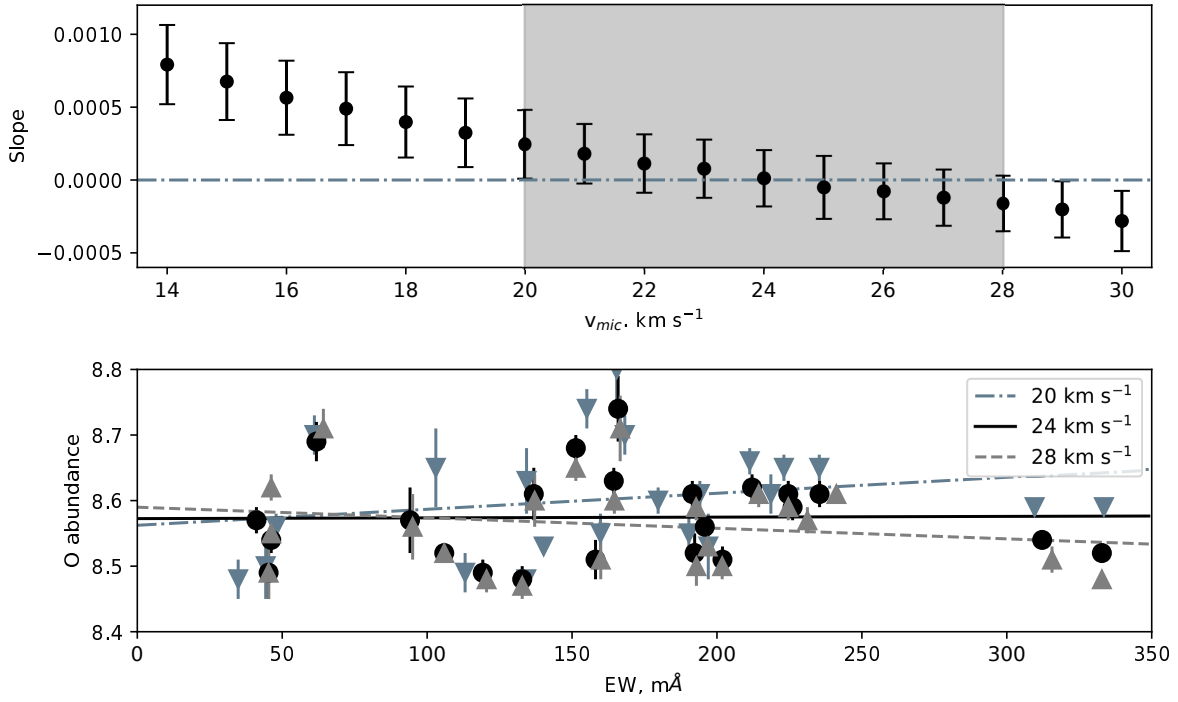


**Figure 9.** The abundance-equivalent width diagram to determine the microturbulence velocity. The top panel shows the dependence of the slope  $\partial(\log \epsilon(O))/\partial(EW)$  on the estimated microturbulence velocity, the bottom panel shows a detailed "EW –  $\epsilon(O)$ " diagram for three values of  $\xi_t = 20, 24, 28 \text{ km s}^{-1}$ .

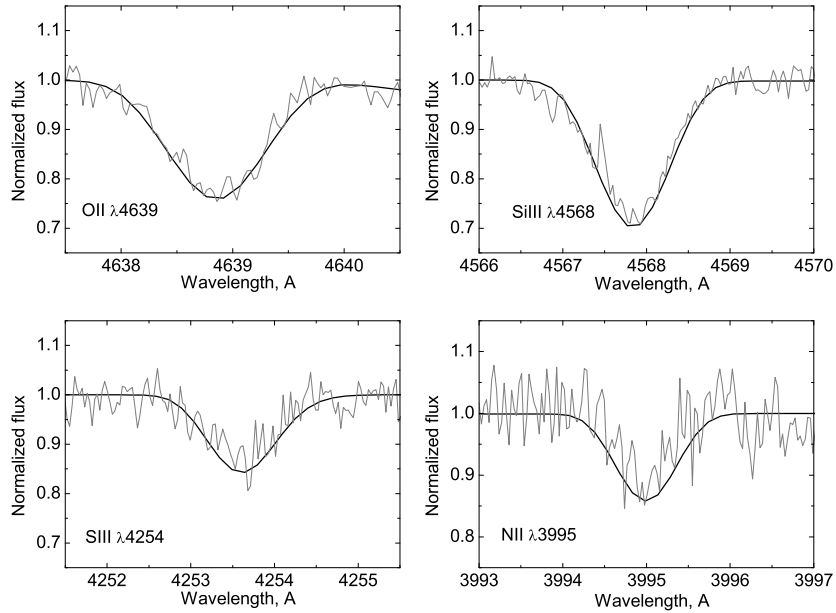


**Figure 10.** The non-LTE theoretical spectra (black lines) are overlaid with the observed profiles (grey lines) of the OII  $\lambda 4639$ , SiIII  $\lambda 4568$ , SiIII  $\lambda 4254$ , and NII  $\lambda 3995$  lines.

over the entire profile is  $\log \varepsilon(C) = 7.73 \pm 0.21$ . In the blue wing of the weak lines  $\lambda 4267$  and  $\lambda 6578$ , there are emission components, so the equivalent widths of these lines cannot be measured. Fitting the red parts of the profiles gives an abundance of  $7.25 \pm 0.25$ . The profile of CII  $\lambda 6583$  is blended with the forbidden line NII  $\lambda 6584$ . Fitting the profile of the CIII  $\lambda 4647$  line gives a higher carbon abundance value of  $\sim 8.0$ . The equivalent width of this line,  $EW=82$  mÅ, results in an abundance value of  $7.84 \pm 0.19$ . Therefore, to determine the abundance, we used only two lines, CII  $\lambda 3919$  and CIII  $\lambda 4647$ , and obtained an average value of  $\log \varepsilon(C) = 7.79$ , which is significantly lower than the solar abundance.

As is well known, the atmospheres of post-AGB stars are often depleted in iron because it is part of the dust in their envelopes and therefore cannot be used to determine the metallicity (Mathis & Lamers 1992). As an alternative, the initial metallicities of stars can be estimated based on the abundance of sulfur (Stasińska *et al.* 2006). As we determined, the sulfur content in LS4331's atmosphere is estimated to be  $[S/H]=-0.81 \pm 0.06$ , hence we can accept  $Z = 0.002$ .

#### 4.5 Rotational velocity

The rotational velocity  $v \sin i$  was determined by comparing the averaged absorption profile with synthetic profiles using Fourier transformation (Smith & Gray 1976). To construct the average profile we used five lines with complete profiles with no distortions: SiIII  $\lambda 4552$ ,  $\lambda 4568$ ,  $\lambda 4575$ ,  $\lambda 5740$  and OI  $\lambda 4591$ . On Fig. 12 the obtained average profile and the synthetic profile for the rotation velocity  $35 \text{ km s}^{-1}$  are presented. The first zero of the Fourier transform of the average profile corresponds to the first zero of the Fourier transform for the synthetic spectrum corresponding to the case of  $35 \text{ km/s}$ . To estimate the error in the determination of  $v \sin i$  we used synthetic observations generated based on the optimal synthetic profile with  $\sigma = 0.015$  by the Monte-Carlo method (a similar approach was used in our work on LS 5112 (Ikonnikova *et al.* 2020)). The final value of  $v \sin i$  we estimate as  $35 \pm 7 \text{ km s}^{-1}$ .

### 5. Analysis of the emission spectrum

Due to the rather low temperature of the central star, the spectrum of the object still contains a quite limited set of lines that are usually used for gas envelope diagnostics. Furthermore, without a

calibrated flux spectrum, it is not possible to obtain reliable absolute fluxes of emission lines. However, using the equivalent widths of emission lines from Appendix B. and the distribution of stellar continuum fluxes for the above-mentioned atmospheric parameters, we can reliably obtain ratios of fluxes in emission lines.

#### 5.1 Nebular parameters

From the available diagnostic line ratios, all densities and temperatures were calculated with the code PYNEB (Luridiana *et al.* 2015). PYNEB routine *getCrossTemden* was used to determine simultaneously the temperature and the density from the [NI], [NII], [OII] and [SII] lines, by building diagnostic diagrams.

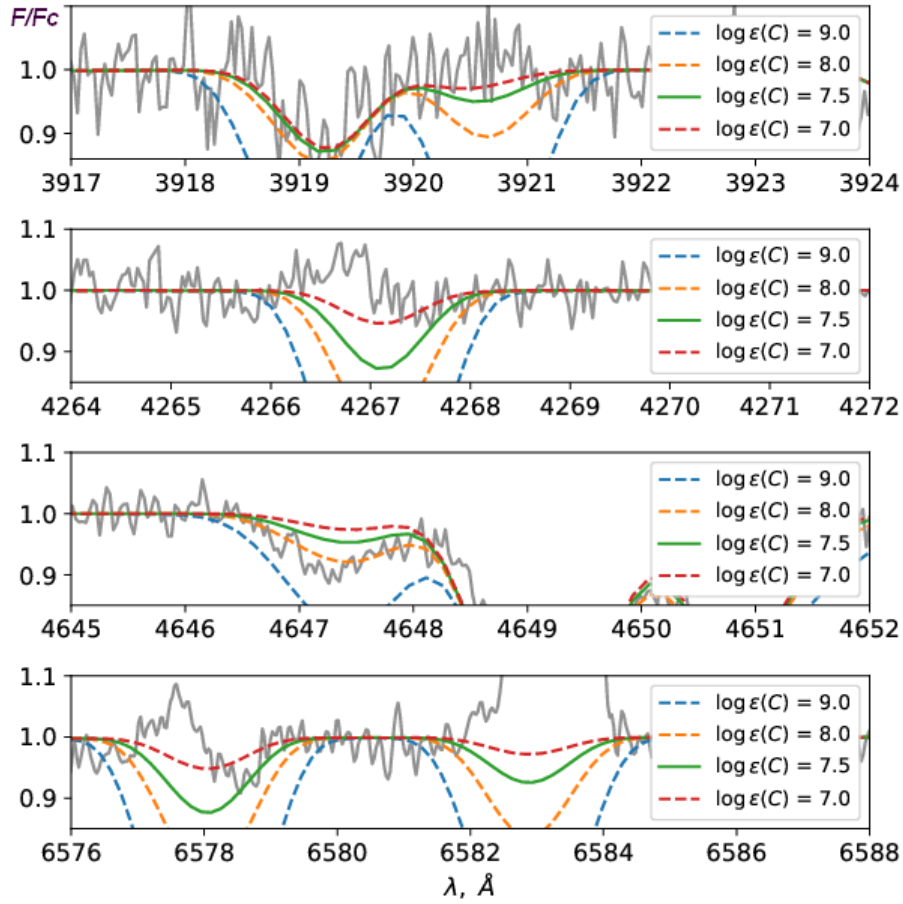
Densities can be determined from the [NI]  $\lambda\lambda 5198/5200$ , [SII]  $\lambda\lambda 6717/6731$  and [OII]  $\lambda\lambda 3726/3729$  intensity ratios. Electron temperatures can be obtained from the [NII]  $\lambda\lambda(6548+6548)/5755$ , [SII]  $\lambda\lambda(4069+4076)/(6717+6731)$  and [OII]  $\lambda\lambda(3726+3729)/(7319+7330)$  intensity ratios.

Fig. 13 displays diagnostic diagram obtained using PYNEB. In the  $T_e$  range from 7000 to 20 000 K and  $\log N_e$  ( $\text{cm}^{-3}$ ) from 1 to 6, the curves have intersection. The nebular line ratios for [NI] indicates that these lines are formed in a partial ionized region of  $N_e \sim 3000 \text{ cm}^{-3}$ , whereas [SII] and [NII] intersection display electron density  $N_e \sim 10000 \text{ cm}^{-3}$ . The electron temperature of the nebula for this region is estimated at  $T_e = 8300-8800 \text{ K}$ .

#### 5.2 Radial and expansion velocities of the gaseous nebula

As a reminder, the stellar radial velocity, determined from absorption lines, is equal to about  $-52 \text{ km s}^{-1}$  (subsection 4.1). The nebular radial velocity obtained from emission lines is  $-60.3 \pm 4.7 \text{ km s}^{-1}$  (Appendix B.). If the shell had a spherical structure, these velocities should have been the same. The difference suggests that the shape of the nebula deviates from spherical. In support of this conclusion, we can point to the finding by Cerigone *et al.* (2008) that the nebula at radio maps at 8.4 GHz observed in high angular resolution has a morphology that resembles a bipolar structure.

To calculate the expansion velocity of the gaseous envelope, we used eight of the strongest and most reliably measured forbidden emission lines. We used the following formula:  $V_{\text{exp}} = 1/2 \sqrt{V_{\text{FWHM}}^2 - V_{\text{instr}}^2}$ , where  $V_{\text{FWHM}}$  is the veloc-



**Figure 11.** Observed CII ( $\lambda$  3919, 4267, 6578) and CIII ( $\lambda$ 4647) line profiles and synthetic ones for various  $\log \epsilon(C)$ .

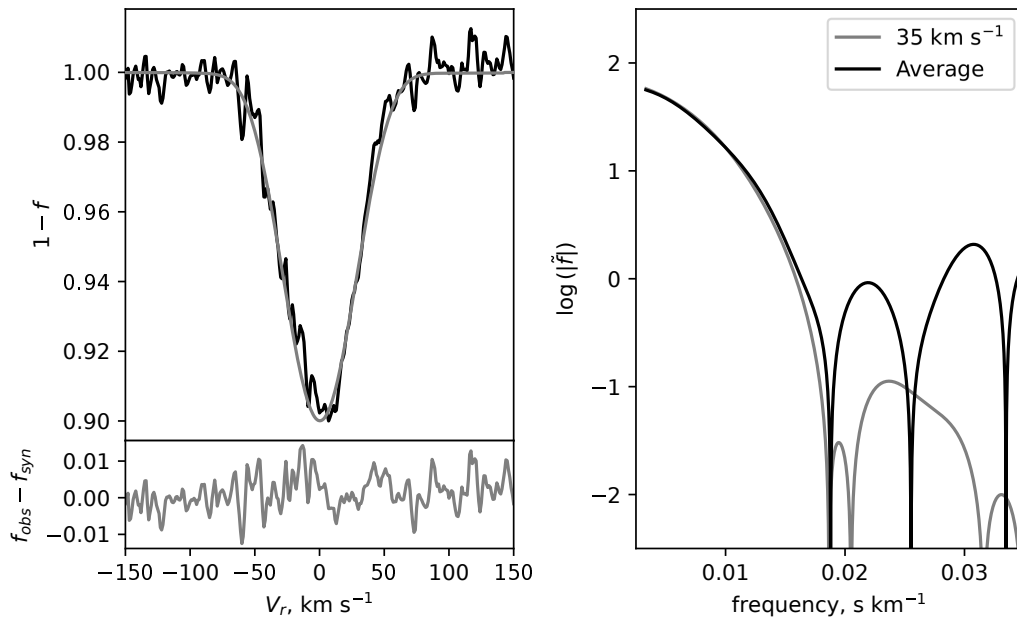


**Figure 12.** The average profile (the left panel) and corresponding Fourier transforms (the right panel). The black lines are for observations, the grey lines are for the synthetic spectrum for  $v \sin i = 35 \text{ km s}^{-1}$ .

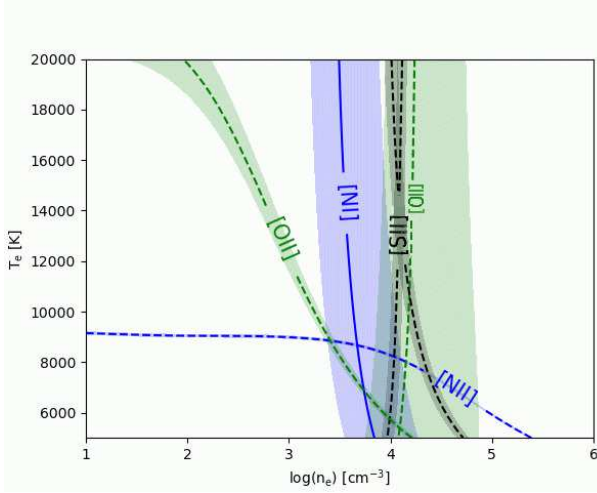


**Figure 13.** Diagnostic diagram for LS 4331, derived with PYNEB.

**Table 4.** Expansion velocities obtained from emission lines.

$\lambda_{obs}$ , Å	$\lambda_{lab}$ , Å	ion	FWHM, Å	$V_{exp}$ , km s <sup>-1</sup>
4286.55	4287.39	[Fe II](7F)	0.46	15.8
6299.04	6300.30	[O I](1F)	0.72	16.8
6546.75	6548.05	[N II](1F)	0.58	12.9
6582.13	6583.45	[N II](1F)	0.58	12.9
6715.12	6716.44	[S II](2F)	0.65	14.2
6729.48	6730.82	[S II](2F)	0.65	14.2
7318.64	7319.99	[O II]	0.70	14.1
9067.12	9068.80	[S III]	0.63	10.0

ity corresponding to the FWHM and  $V_{instr} = 6 \text{ km s}^{-1}$  is the instrumental broadening. The adopted  $V_{exp}$  for each ion are given in Table 4.

Note the difference in the expansion velocity between the less and more ionised species. The highest value was obtained for the [OI] line (16.8 km s<sup>-1</sup>), the lowest for the [SIII] line (10.0 km s<sup>-1</sup>), and intermediate values for [NII], [OII], [SII] and [Fe II] (12.9 – 14.2 km s<sup>-1</sup>). This can be explained by the fact that the ionized shell possesses a layered structure, with more ionized species located closer to the central star. The structure tends to display an expansion velocity gradient, with larger velocities directed towards the external zones, where less-ionized species are found.

## 6. Photometric analysis

As seen in Fig. 14, which shows the light curves in both the *V* and *g* bands, based on the combined

ASAS-SN and RC600 data, the object is clearly variable with peak-to-peak range of brightness variations of about 0.3 mag and 0.4 mag, respectively. The brightness of the star varies significantly from night to night. The behavior of the brightness in the other bands is similar to that of the *V*-band. We conducted a periodogram analysis of the ASAS-SN light curves using the period-finding program Period04 (Lenz & Breger 2005), but did not detect any periodic components in the period range of 0.3-50 days in the full dataset. We also did not detect any periodicity when analyzing the data for each season individually.

The multicolour photometry obtained with the RC600 telescope allowed us to track the change in colour alongside the brightness. Fig. 15 shows the *V*-band light curve and the *B* – *V*, *V* – *R<sub>C</sub>*, *R<sub>C</sub>* – *I<sub>C</sub>* colour curves of the star for three seasons in 2021-2023. As can be seen on Fig. 15, colour indices change both from season to season and within each season. Fig. 16 illustrates the dependencies of the colour indices *B* – *V* and *R<sub>C</sub>* – *I<sub>C</sub>* on the brightness. It can be seen that, as the brightness decreases, *B* – *V* decreases, while *R<sub>C</sub>* – *I<sub>C</sub>* increases, making the star look redder.

Similar variability in brightness and colour *B* – *V* has been observed in our previous research on the study of hot post-AGB stars. For example, IRAS 19200+3457 (Arkhipova *et al.* 2004), V886 Her (Arkhipova *et al.* 2007), IRAS 01005+7910, IRAS 22023+5249 and IRAS 22495+5134 (Arkhipova *et al.* 2013) exhibit rapid variability with a period of a few days and an amplitude of 0.2 to 0.4 mag in the *V* band. So far, no periodic component has been detected in the variability of brightness for any of the objects in our studies. Like LS4331, the other objects mentioned exhibit a decrease in their *B* – *V* colour index when the object dims.

Hot post-AGB stars can be variable in brightness due to various processes that affect their surface and atmosphere, such as pulsation, mass loss, and evolution. Evolutionary changes occur over time scales of several decades, as in the case of V886 Her (Arkhipova *et al.* 2007). Pulsations can also occur, but so far for all of the above objects, a periodic component in the change in brightness has not been identified. Additionally, hot post-AGB stars do not exhibit an increase in their *B* – *V* colour index when their brightness decreases, as is characteristic of pulsating stars. For example, cooler post-AGB stars of spectral type F-G-K, which pulsate, become redder when they fade, indicating a decrease in temperature due to the pulsations (e.g.,

Hrivnak *et al.* 2015; Ikonnikova *et al.* 2023).

Thus, to explain variability with a characteristic time of a fraction of a day or several days and an amplitude of the order of 0.2-0.4 mag, a variable stellar wind remains. According to evolutionary calculations (Miller Bertolami 2016), for a hot post-AGB star with a temperature in the range of 21000 K, an estimated rate of mass loss on the order of  $10^{-8}M_{\odot}$  per year is expected.

## 7. Mass and luminosity

Doubts about LS 4331 belonging to the class of post-AGB stars are not valid. In addition to the main characteristics of this class of objects such as the presence of an excess of emission in the far-infrared region and the shape of the spectral energy distribution, in this work we defined some parameters of the star and its gaseous envelope characteristic of stars in the post-AGB stage of evolution.

To determine the stellar mass, we compared the obtained values of effective temperature and surface gravity with the evolutionary tracks for H-rich post-AGB stars that have been presented by (Miller Bertolami 2016). The closest to the obtained point is the track with the parameters: the initial mass of the progenitor  $M_{ZAMS} = 1.25M_{\odot}$  and the current mass  $M_c = 0.58M_{\odot}$  for initial metallicity  $Z = 0.001$  (Fig. 17). The star with  $T_{\text{eff}} = 21000$  K falls on the horizontal part of the post-AGB evolutionary track on the Hertzsprung-Russell diagram with  $\log(L/L_{\odot}) \sim 3.9$ .

On the one hand, the luminosity of the star can be determined by knowing the distance, the interstellar extinction, and the apparent brightness. The average brightness of  $V$  in our data is  $13.22 \pm 0.07$  mag, while the colour index  $B - V = 0.34 \pm 0.02$ . For a supergiant of effective temperature  $T_{\text{eff}} \approx 21000$  K ( $\log T_{\text{eff}} = 4.32$ ) the normal colour index  $(B - V)_0$  is  $-0.2$  based on the calibration of Flower (1996). Then the colour excess  $E(B - V)$  is  $0.54 \pm 0.02$ . The star in the DR3 catalog has the parallax of  $0.1086 \pm 0.0249$  (Gaia Collaboration *et al.* 2021). The median of the photogeometric distance derived from this parallax is  $d = 8256^{+1049}_{-819}$  pc (Bailer-Jones *et al.* 2021). According to the known formula for absolute stellar magnitude  $M_V = V + 5 - 5 \log d - A_V$ , where  $A_V$  is the extinction in  $V$  band, calculated as  $A_V = 3.1E(B - V)$ , we find  $M_V \approx -3.04$ . For a star of effective temperature  $T_{\text{eff}} \approx 21000$  K according to a calibration of Flower (1996) the bolometric correction is estimated to be  $BC = -2.0$ , and

thus the absolute bolometric magnitude is given by  $M_{\text{bol}} = M_V + BC \approx -5.04$  and  $\log(L/L_{\odot})$  can be calculated as  $\log(L/L_{\odot}) = (M_{\text{bol}\odot} - M_{\text{bol}})/2.5 \approx 3.90$ . This evaluation is in close agreement with that obtained by comparing with evolutionary models.

It should be taken into account that both luminosity estimates are burdened with significant errors. In the case of an estimate obtained by comparing the parameters of the star with evolutionary models, the evolutionary track we have chosen does not fully agree with the characteristics of the star, since its metallicity  $Z = 0.002$  is slightly higher than that accepted for the model ( $Z = 0.001$ ). Calculations for  $Z = 0.002$  are not presented in Miller Bertolami (2016). In addition, the parameters of the star ( $\log T_{\text{eff}}$  and  $\log g$ ), which were compared to evolutionary tracks, also have some errors associated with them. Also, each of the quantities included in the formula for calculating the absolute magnitude (primarily distance) has significant errors.

## 8. DISCUSSION

Our analysis of the high-resolution optical spectrum of LS 4331 together with our detailed line identifications confirms that LS4331 is an evolving hot post-AGB star. The chemical composition of LS 4331 reported in this study clearly indicates that it is metal-poor and O-rich similar to that found in some of the hot post-AGB stars (Moehler & Heber 1998, Ryans *et al.* 2003 and references therein) and indicates that its AGB phase of evolution may have been terminated before the third dredge up. We concluded that LS4331 is metal-poor based on the following facts: firstly, the iron lines are extremely weak, and we were unable to measure their equivalent widths to determine the chemical composition. Additionally, the abundance of elements such as Mg, Al, and S is significantly lower than solar (Table 3). The carbon lines are weak and the carbon abundance is determined with uncertainty, while the oxygen abundance is measured reliably and is close to the solar value. Thus, our study confirms the conclusion of Cerrigone *et al.* (2009) that LS4331 is an O-rich object, similar to some other hot post-AGB objects, such as IRAS 17074-1845, IRAS 17203-1534, IRAS 17460-3114, and IRAS 18062+2410 (Cerrigone *et al.* 2009), for the first three of which Mello *et al.* (2012), and for IRAS 18062+2410 Ryans *et al.* (2003) determined the chemical composition and confirmed that in their stellar atmospheres

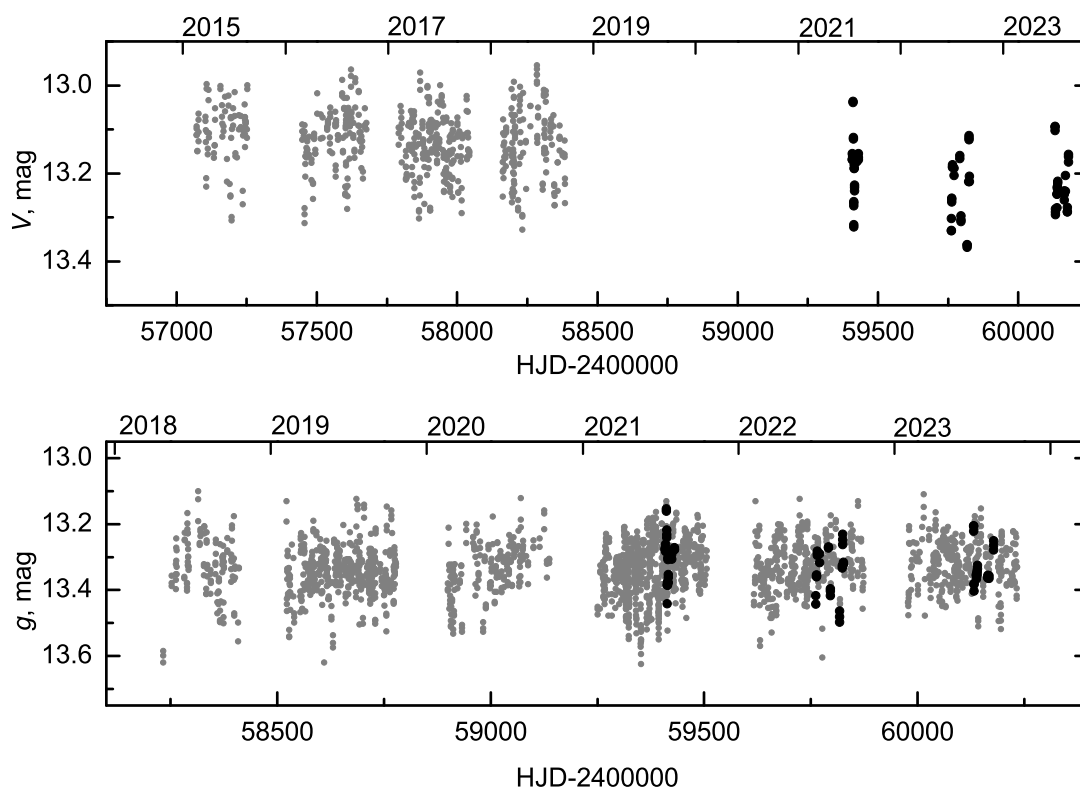


**Figure 14.** The light curves of ASAS-SN (grey circles) and RC600 (black circles) data in V-band (top panel) and g-band (bottom panel).

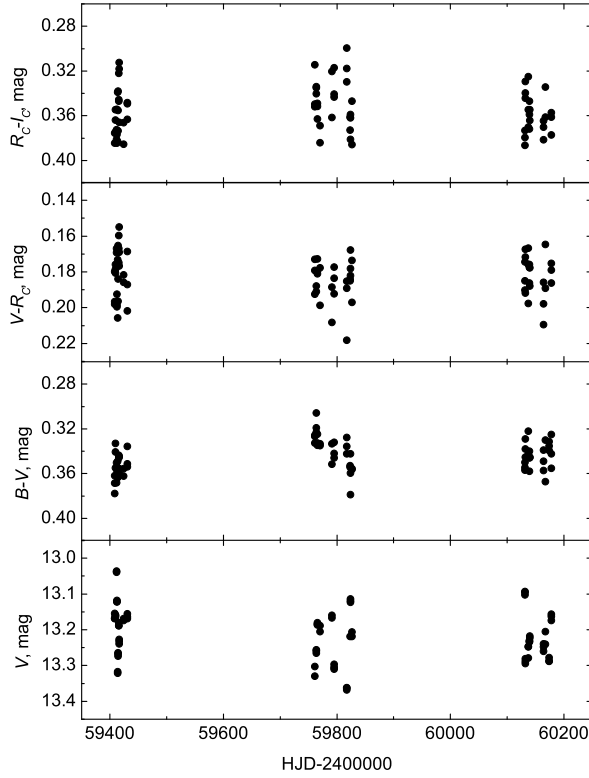


**Figure 15.** The light and colour curves of RC600 data in 2021–2023.

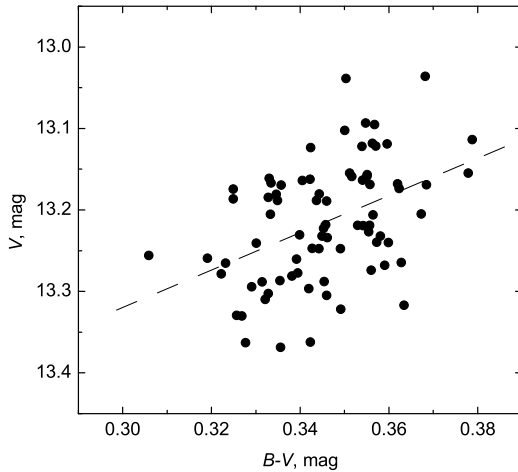


**Figure 16.** Plots showing the change in colour with change in brightness. The object shows a trend of becoming bluer when it fainter. The dashed line represents a linear fit to the data.

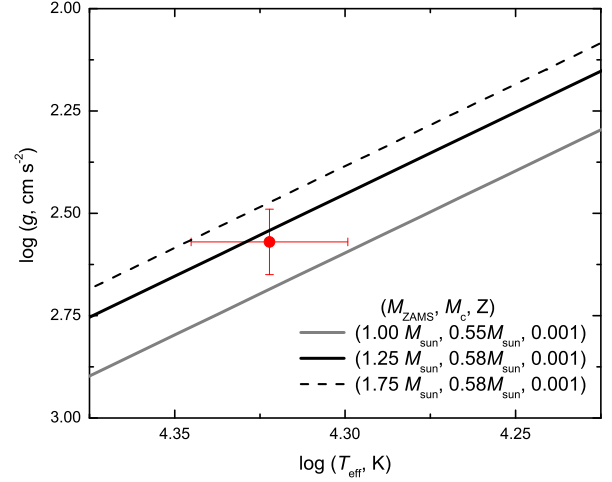


**Figure 17.** Location of LS 4331 (the red circle) in the  $T_{\text{eff}}\text{-log } g$  plane with  $Z = 0.001$  single-star evolutionary tracks of Miller Bertolami (2016).

$C/O < 1$ . Examples of hot O-rich post-AGB objects also include IRAS 19590-1249 (Ryans *et al.* 2003, Mello *et al.* 2012), PG 1323-086 and PG 1704+222 (Moehler & Heber 1998), and IRAS 18379–1707 (Ikonnikova *et al.* 2020).

To determine the iron abundance in the stellar atmosphere, high-resolution spectral observations in the ultraviolet (UV) region would be useful. Such work has been done for post-AGB stars in globular clusters: ROA 5701 in  $\omega$  Centauri and Barnard 29 in M 13. For these stars, the UV observations are from the Goddard high-resolution spectrograph on the Hubble Space Telescope (HST). The UV data provide additional Fe abundance estimates from Fe III absorption lines in the 1875–1900 Å wavelength region (Thompson *et al.* 2007).

The analysis of the high-resolution spectrum did not reveal any signs of the presence of a second component in the system. However, for a more conclusive conclusion about the absence of binarity, a long-term spectral monitoring is necessary, which would allow to construct a radial velocity curve.

The effective temperature of the star ( $T_{\text{eff}} \approx 21000$  K) is high enough to ionize the gaseous envelope surrounding the star. Analysis of the emission spectrum of the star allowed us to estimate the parameters of the gas envelope.

The discovery of rapid irregular photometric variability in LS 4331 is an important result of our work. Currently, about 15 objects with similar photometric characteristics are known (for



example, V1853 Cyg (Turner & Drilling 1984, Arkhipova *et al.* 2001), V886 Her (Arkhipova *et al.* 2007), IRAS 07171+1823 (Arkhipova *et al.* 2006), IRAS 19306+1407 (Hrivnak *et al.* 2020) etc), which allows us to consider this to be a common property of hot post-AGB stars. The nature of this variability is still not well understood, and further photometric and spectroscopic observations are necessary to study the physical processes occurring in the atmospheres of these stars.

## 9. CONCLUSIONS

We have presented a non-LTE analysis of high resolution optical spectrum, and photometric variability of LS 4331, a hot post-AGB star whose spectral properties and photometric behavior had not been investigated before in detail. Our conclusions can be summarized as follows:

1) We identified the spectrum in the wavelength range of 3600-9500 Å for the first time. The spectrum contains numerous absorption lines belonging to the star and emission lines from the surrounding gas envelope.

2) We determined the parameters of the star: effective temperature  $T_{\text{eff}} = 20900 \pm 500$  K, surface gravity  $\log g = 2.57 \pm 0.08$ , radial velocity  $V_r = -51.7 \pm 0.8$  km s<sup>-1</sup>, and micro-turbulent velocity  $\xi_t = 24 \pm 4$  km s<sup>-1</sup>.

3) We determined the composition of 7 elements ([C/H]=-0.64 dex, [N/H]=-0.38 dex, [O/H]=-0.12 dex, [Mg/H]=-1.04, [Al/H] = -1.20 dex, [Si/H] = -0.46 dex, [S/H] = -0.81 dex) and confirmed the conclusion that the star is rich in oxygen and poor in carbon and metals.

4) The star already has a high enough temperature to ionise its envelope, and we estimated parameters  $T_e = 5000$  K and  $N_e = 3000 - 5000$  cm<sup>-3</sup> for it.

5) By comparing with theoretical evolutionary tracks, we determined the initial mass  $M_{\text{ZAMS}} \sim 1.25M_{\odot}$  and the current mass  $M_c \sim 0.58M_{\odot}$  of the star. The estimated luminosity in the range of  $L = 5600 - 7300 L_{\odot}$  is obtained both by comparison with theoretical evolutionary sequences and by using distance measurements from the Gaia DR3.

6) Analysis of the light curves obtained in the ASAS-SN survey and by us on the RC600 telescope showed that the star experiences irregular brightness fluctuations with a full amplitude of about 0.3 mag in the V band and a typical period of about one to several days. It is hypothesized that the variability in brightness is related to the variable

stellar wind. We estimated the colour excess to be  $E(B - V) = 0.54 \pm 0.02$ .

## Acknowledgement

This research has used the SIMBAD data base, operated at CDS, Strasbourg, France, and SAO/NASA Astrophysics Data System. We are thankful to the referee very much for useful comments and constructive suggestions.

## References

- Arkhipova V.P., Ikonnikova N.P., Noskova R.I., Komissarova G.V., Klochkova V.G., Esipov V.F., 2001, *Astron. Lett.*, 27, 719
- Arkhipova V.P., Ikonnikova N.P., Noskova R.I., Esipov V.F., 2004, *Astron. Lett.* 30, 778
- Arkhipova V.P., Klochkova V.G., Chentsov E.L., Esipov V.F., Ikonnikova N.P., Komissarova G.V., 2006, *Astron. Lett.*, 32, 661
- Arkhipova V.P., Esipov V.F., Ikonnikova N.P., Komissarova G.V., Noskova R.I., 2007, *Astron. Lett.*, 33, 604
- Arkhipova V.P., Burlak M.A., Esipov V.F., Ikonnikova N.P., Komissarova G.V., 2013, *Astron. Lett.*, 39, 619
- Arkhipova V.P., Parthasarathy, M., Ikonnikova N.P., Ishigaki M., Hubrig S., Sarkar G., Kniazev A.Y., 2018, *MNRAS*, 481, 3935
- Asplund M., Grevesse N., Sauval A.J., Scott P., 2009, *ARAA*, 47, 481
- Bailer-Jones C.A.L., Rybizki J., Fouesneau M., Demleitner M., Andrae R., 2021, *Astron. J.*, 161, 147
- Berdnikov L.N., Belinskii A.A., Shatskii N.I., Burlak M.A., Ikonnikova N.P., Mishin E.O., Cheryasov D.V., Zhuiko S.V., 2020, *Astron. Rep.*, 64, 310
- Cerrigone L., Umama G., Trigilio C., Leto P., Buemi C.S., Hora J.L., 2008, *MNRAS*, 390, 363
- Cerrigone L., Hora J.L., Umama G., Trigilio C., 2009, *Astrophys. J.*, 703, 585
- Cerrigone L., Trigilio C., Umama G., Buemi C.S., Leto P., 2011, *MNRAS*, 412, 1137
- Collins K.A., Kielkopf J.F., Stassun K.G., Hessman F.V., 2017, *Astron. J.*, 153, 77
- Flower P.J., 1996, *Astrophys. J.*, 469, 355
- Gaia Collaboration et al., 2021, *Astron. Astrophys.*, 649, A1
- García-Lario P., Parthasarathy M., de Martino D., Sanz Fernández de Córdoba L., Monier R., Machado A., Pottasch S. R., 1997, *Astron. Astrophys.*, 326, 1103

- Herrero A., Parthasarathy M., Simón-Díaz S.; Hubrig S., Sarkar G., Muneer S., 2020, *MNRAS*, 494, 2117
- Hrivnak B.J., Lu W., and Nault K.A., 2015, *Astron. J.*, 149, 184
- Hrivnak B. J., Henson G., Hillwig T.C., Lu W., Nault K.A., Volk K., 2020, *Astrophys. J.*, 901, 9
- Hobbs L.M., York D.G., Snow T.P., Oka T., Thorburn J.A., Bishof M., Friedman S.D., McCall B.J., Rachford B., Sonnentrucker P., Welty D.E., 2008, *Astrophys. J.*, 680, 1256
- Hubeny I., Lanz T., 1995, *Astrophys. J.*, 439, 875
- Ikonnikova N.P., Parthasarathy M., Dodin A.V., Hubrig S., Sarkar G., 2020, *MNRAS*, 491, 4829
- Ikonnikova N.P., Burlak M.A., Dodin A.V. et al., 2023, *Astrophysical Bulletin*, 78, 348
- Kaufer A., Stahl O., Tubessing S. et al., 1999, *The Messenger*, 95, 8
- Kausch W., Noll S., Smette A., Kimeswenger S., Barden M., Szyszka C., Jones A.M., Sana H., Horst H., Kerber F., 2015, *Astron. Astrophys.*, 576, A78.
- Klochkova V.G., Yushkin M.V., Miroshnichenko A.S., Panchuk V.E., Bjorkman K.S., 2002, *Astron. Astrophys.*, 392, 143
- Kochanek C.S., Shappee B.J., Stanek K.Z., Holoiien T.W.-S., Thompson, Todd A. et al., 2017, *PASP*, 129:104502
- Lenz P., Breger M., 2005, *CoAst*, 146, 53
- Luridiana V., Morisset C., Shaw R.A., 2015, *Astron. Astrophys.*, 573, 42
- Mathis J.S., Lamers H.J.G.L.M., 1992, *Astron. Astrophys.*, 259, 39
- Mello D.R.C., Daflon S., Pereira C.B., Hubeny I., 2012, *Astron. Astrophys.*, 543, A11
- Miller Bertolami M.M., 2016, *Astron. Astrophys.*, 588, A25
- Moehler S., Heber U., 1998, *Astron. Astrophys.*, 335, 985
- Mooney C.J., Rolleston W.R.J., Keenan F.P., Dufton P. L., Smoker J.V., Ryans R.S.I., Aller L.H., 2002, *MNRAS*, 337, 851
- Otsuka M., Parthasarathy M., Tajitsu A., Hubrig S., 2017, *Astrophys. J.*, 838, 71
- Parthasarathy M., Pottasch S.R., 1986, *Astron. Astrophys.*, 154, L16
- Parthasarathy M., Pottasch S.R., 1989, *Astron. Astrophys.*, 225, 521
- Parthasarathy M., 1993, *Astrophys. J.*, 414, L109
- Parthasarathy M., 1994, *ASPC*, 60, 261
- Parthasarathy M., Vijapurkar J., Drilling J.S., 2000, *Astron. Astrophys. Suppl. Ser.*, 145, 269
- Parthasarathy M., Matsuno T., Aoki W., 2020, *PASJ* 72, 99
- Ryans R.S.I., Dufton P.L., Mooney C.J., Rolleston W.R.J., Keenan F.P., Hubeny I., Lanz T., 2003, *Astron. Astrophys.*, 401, 1119
- Sarkar G., Parthasarathy M., Reddy B.E., 2005, *Astron. Astrophys.*, 431, 1007
- Shappee B.J., Prieto J.L., Grupe D., Kochanek C.S., Stanek K. Z., De Rosa G., 2014, *Astrophys. J.*, 788, 48
- Smith M.A., Gray D.F., 1976, *PASP*, 88, 809
- Stasińska G., Szczerba R., Schmidt M., Siódmiak N., 2006, *Astron. Astrophys.*, 450, 701
- Stephenson C.B., Sanduleak N., 1971, *Publ. Warner and Swasey Obs.*, 1, part no 1, 1
- Suárez O., García-Lario P., Manchado A. et al., 2006, *Astron. Astrophys.*, 458, 173
- Thompson H.M.A., Keenan F.P., Dufton P.L., Ryans R.S.I., Smoker J.V., Lambert D. L., Zijlstra A.A., 2007, *MNRAS*, 378, 1619
- Turner D.G., Drilling J.S., *PASP*, 1984, 96, 292
- Zachariah N., Finch C.T., Girard T.M., Henden A., Bartlett J.L., Monet D.G., Zacharias M.I., 2013, *Astron. J.*, 145, 44

**Appendix A. Multicolour photometry of LS 4331****Table 5:** Multicolour photometry of LS 4331.

HJD	<i>B</i>	<i>V</i>	<i>R<sub>C</sub></i>	<i>I<sub>C</sub></i>	<i>g</i>	<i>r</i>	<i>i</i>
2459408.325	13.530	13.168	12.970	12.594	13.272	12.967	12.982
2459408.329	13.533	13.155	12.975	-	13.276	12.975	12.959
2459408.332	13.538	13.169	12.973	12.588	13.279	12.973	12.978
2459409.293	13.494	13.161	12.982	12.628	13.277	12.982	13.012
2459409.296	13.514	13.159	12.983	12.608	13.261	12.983	13.001
2459409.299	13.504	13.164	12.983	12.619	13.283	12.983	13.005
2459411.277	13.404	13.036	12.869	12.496	13.161	12.869	12.887
2459411.280	13.389	13.039	12.869	12.488	13.154	12.869	12.896
2459412.262	13.474	13.118	12.926	12.549	13.218	12.926	12.922
2459412.265	13.476	13.122	12.923	12.569	13.232	12.923	12.923
2459412.268	13.478	13.121	12.922	12.538	13.241	12.922	12.927
2459413.301	13.671	13.322	13.116	12.777	13.441	13.116	13.161
2459413.305	13.680	13.317	13.144	12.760	13.384	13.144	-
2459414.295	13.630	13.274	13.077	12.722	13.385	13.077	13.119
2459414.298	13.627	13.265	13.081	12.742	13.377	13.080	13.121
2459414.301	13.627	13.268	13.102	12.729	13.376	13.102	13.118
2459415.296	13.535	13.189	13.022	12.675	13.301	13.022	-
2459415.300	13.525	13.180	13.020	12.698	13.302	13.020	13.058
2459415.303	13.532	13.188	13.014	12.668	13.308	13.014	-
2459416.294	13.582	13.227	13.072	12.706	13.378	13.072	-
2459416.297	13.600	13.240	13.071	12.758	13.362	13.071	-
2459416.300	13.577	13.232	13.055	12.737	13.353	13.055	-
2459424.254	13.524	13.169	12.987	12.602	13.307	12.987	13.002
2459424.257	13.536	13.174	12.988	12.621	13.291	12.988	12.990
2459430.272	13.518	13.164	12.962	12.612	13.277	12.962	13.012
2459430.275	13.506	13.155	12.986	12.623	13.272	12.986	13.017
2459430.278	13.505	13.169	12.982	12.634	13.277	12.982	13.001
2459761.329	13.636	13.303	13.130	12.815	13.417	13.130	13.171
2459761.332	13.657	13.330	13.151	12.799	13.417	13.151	13.175
2459761.335	13.655	13.330	13.137	12.788	13.443	13.137	13.183
2459763.377	13.562	13.256	13.076	12.741	13.360	13.076	13.135
2459763.380	13.578	13.259	13.071	12.731	13.354	13.071	13.113
2459763.383	13.588	13.265	13.074	12.740	13.357	13.074	13.140
2459765.327	13.517	13.185	13.005	12.656	13.288	13.005	13.031
2459765.330	13.511	13.187	13.006	12.654	13.295	13.006	13.027
2459765.333	13.515	13.181	13.008	12.645	13.282	13.008	13.029
2459770.318	13.539	13.205	13.006	12.638	13.290	13.006	13.044
2459770.322	13.523	13.188	13.010	12.626	13.317	13.010	13.037
2459791.282	13.511	13.159	12.970	12.609	13.273	12.970	12.997
2459791.285	13.500	13.167	12.959	12.638	13.268	12.959	12.985
2459795.249	13.651	13.305	13.121	12.778	13.396	13.121	13.166
2459795.252	13.642	13.310	13.117	12.800	13.417	13.118	13.154
2459795.255	13.638	13.297	13.119	12.779	13.403	13.119	13.161
2459817.248	13.690	13.363	13.174	12.856	13.463	13.174	13.233
2459817.249	13.704	13.368	13.150	12.851	13.481	13.150	13.242
2459817.250	13.704	13.362	13.177	12.847	13.498	13.177	13.245
2459823.216	13.573	13.219	13.034	12.661	13.333	13.034	13.045
2459823.219	13.572	13.219	13.035	12.673	13.326	13.035	13.045
2459824.199	13.466	13.123	12.945	12.584	13.262	12.945	12.949
2459824.200	13.492	13.114	12.931	12.573	13.230	12.931	12.950
2459824.201	13.479	13.119	12.951	12.570	13.246	12.951	12.952

continued Table 5

HJD	<i>B</i>	<i>V</i>	<i>R<sub>C</sub></i>	<i>I<sub>C</sub></i>	<i>g</i>	<i>r</i>	<i>i</i>
2459826.197	13.574	13.219	13.022	12.675	13.321	13.022	–
2459826.201	13.563	13.206	13.033	12.647	13.315	13.032	–
2460131.330	13.448	13.093	12.919	12.539	13.221	12.919	12.928
2460131.333	13.452	13.102	12.912	12.539	13.205	12.912	12.918
2460131.336	13.452	13.095	12.910	12.524	13.206	12.910	12.931
2460132.369	13.633	13.288	13.116	12.772	13.380	13.116	13.157
2460132.372	13.619	13.281	13.114	12.774	13.383	13.114	13.146
2460132.375	13.623	13.294	13.102	12.773	13.403	13.102	13.159
2460137.310	13.592	13.248	13.081	12.756	13.353	13.081	13.148
2460137.313	13.601	13.278	13.081	12.726	13.357	13.081	13.141
2460137.316	13.590	13.247	13.071	12.701	13.367	13.071	13.12
2460139.322	13.590	13.232	13.056	12.697	13.355	13.056	13.071
2460139.326	13.580	13.234	13.056	12.685	13.342	13.056	13.092
2460139.329	13.570	13.230	13.044	12.697	13.347	13.044	13.064
2460140.306	13.568	13.223	13.035	12.680	13.325	13.035	13.076
2460140.309	13.564	13.218	13.040	12.676	13.336	13.040	13.064
2460164.248	13.599	13.260	13.051	12.669	13.355	13.051	13.066
2460164.251	13.597	13.240	13.054	12.684	13.364	13.054	13.063
2460164.254	13.597	13.248	13.050	12.685	13.363	13.050	13.083
2460167.256	13.572	13.205	13.040	12.679	13.364	13.040	13.106
2460167.259	13.571	13.241	13.052	12.717	13.356	13.052	13.095
2460174.239	13.619	13.288	–	12.763	–	–	–
2460174.242	13.622	13.287	–	12.749	–	–	–
2460174.246	13.617	13.277	–	12.738	–	13.014	–
2460178.232	13.504	13.162	12.987	12.610	13.265	12.987	13.032
2460178.235	13.512	13.157	12.978	12.617	13.278	12.978	13.005
2460178.238	13.499	13.174	12.988	12.631	13.250	12.988	13.015

**Appendix B. Emission lines in the spectrum of LS 4331****Table 6:** Emission lines in the spectrum of LS 4331.

$\lambda_{\text{obs.}}, \text{\AA}$	$\lambda_{\text{lab.}}, \text{\AA}$	Identification	$EW, \text{m\AA}$	$\sigma_{EW}, \text{m\AA}$	$V_r, \text{km s}^{-1}$
3728.07	3728.82	[O II]	1497	137	-60.30
3725.30	3726.03	[O II]	3529	149	-58.74
3728.07	3728.82	[O II]	1497	137	-60.30
4067.79	4068.59	[S II]	408	47	-58.9
4243.19	4243.98	[Fe II](21F)	83	13	-55.8
4286.55	4287.39	[Fe II](7F)	226	11	-58.7
4339.59	4340.47	H I	1996	20	-60.4
4358.46	4359.34	[Fe II](7F)	185	17	-60.5
4367.40	4368.13	O I(5)	152	21	-50.0
4412.87	4413.78	[Fe II](6F)	203	23	-61.7
4813.53	4814.55	[Fe II](20F)	119	21	-63.5
4860.35	4861.28	H I	5693	27	-57.4
5039.98	5041.03	Si II(5)	134	12	-62.4
5054.93	5055.98	Si II(5)	253	9	-62.2
5126.24	5127.35	Fe III(5)	68	8	-64.8
5157.74	5158.75	Fe III(5)	159	11	-58.6
5196.83	5197.90	[N I](1F)	111	9	-61.7
5199.26	5200.26	[N I](1F)	53	6	-57.6
5242.02	5243.31	Fe III	46	4	-73.7
5260.56	5261.61	[Fe II](19F)	128	8	-59.8
5272.22	5273.35	[Fe II](18F)	75	5	-64.2
5297.98	5298.97	O I(26)	86	7	-56.0
5511.65	5512.77	O I(25)	54	5	-60.9
5553.87	5554.95	O I(24)	65	6	-58.2
5753.44	5754.59	[N II](2D)	144	8	-59.9
5956.34	5957.56	Si II(4)	104	5	-61.4
5957.30	5958.58	O I	118	6	-64.4
5977.72	5978.93	Si II(4)	239	7	-60.6
6031.08	6032.67	Fe III	58	8	-79.0
6045.17	6046.38	O I(22)	242	8	-59.9
6299.04	6300.30	[O I](1F)	431	7	-59.9
6345.77	6347.11	Si II(2)	381	7	-63.2
6362.55	6363.78	[O I](1F)	126	6	-57.9
6370.05	6371.37	Si II(2)	162	5	-62.1
6546.75	6548.05	[N II](1F)	5270	25	-59.5
6561.49	6562.82	H I	44412	178	-60.6
6582.13	6583.45	[N II](1F)	16070	70	-60.1
6715.12	6716.44	[S II](2F)	1042	10	-58.9
6729.48	6730.82	[S II](2F)	2200	14	-59.6
7000.71	7002.13	O I(21)	317	6	-60.7
7153.66	7155.17	[Fe II]	101	18	-63.2
7229.69	7231.03	C II(3)	233	7	-55.5
7234.84	7236.02	C II(3)	317	5	-48.8
7252.96	7254.36	O I(20)	292	9	-57.8
7317.53	7318.99	[O II]	105	35	-59.8
7318.64	7319.99	[O II]	960	8	-55.2
7328.23	7329.67	[O II]	510	8	-58.8
7329.29	7330.73	[O II]	500	15	-58.8
7376.42	7377.83	[Ni II](2F)	372	18	-57.3
7410.16	7411.61	[Ni II](2F)	122	14	-58.6
7466.81	7468.31	N I(3)	215	7	-60.2

continued Table 6

$\lambda_{\text{obs.}}, \text{\AA}$	$\lambda_{\text{lab.}}, \text{\AA}$	Identification	$EW, \text{m\AA}$	$\sigma_{EW}, \text{m\AA}$	$V_r, \text{km s}^{-1}$
7894.45	7896.37	Mg II(8)	78	7	-72.8
7998.29	8000.07	[Cr II](1F)	88	6	-66.6
8123.62	8125.30	[Cr II](1F)	52	6	-61.9
8240.66	8242.34	N I(7)	291	14	-61.0
8299.81	8301.59	[Ni II](2F)	250	40	-64.2
8444.79	8446.25	O I(3)	6090	19	-51.8
8701.50	8703.25	N I(1)	221	15	-60.2
8709.93	8711.70	N I(1)	268	16	-60.9
9067.12	9068.80	[S III]	1629	14	-55.5

**Appendix C. Radial velocities and elemental abundances of the stellar absorption lines****Table 7:** Absorption lines used for measurement of the stellar radial velocity and elemental abundances.

Ion	$\lambda_{lab}$ , Å	$\lambda_{obs}$ , Å	$E_l$ , eV	EW, mÅ	$\sigma_{EW}$ , mÅ	$\log \epsilon$	$\sigma_{\log \epsilon}$	$V_r$ , km s <sup>-1</sup>	$\sigma_{V_r}$ , km s <sup>-1</sup>
N II	3995.00	3994.29	18.5	135.4	15.0	7.48	0.04	-53.0	2.3
N II	5001.48	–	20.7	38.0	10.3	7.20	0.05	–	–
N II	5045.10	–	18.5	51.6	9.1	7.90	0.03	–	–
N II	5666.62	5665.79	18.5	50.2	4.5	7.20	0.03	-44.3	1.6
N II	5676.02	5675.13	18.5	52.1	5.0	7.56	0.02	-46.9	1.7
N II	5679.59	5678.80	18.5	92.4	5.0	7.77	0.03	-40.1	1.2
O II	3911.97	3911.21	25.7	136.8	12.0	8.59	0.04	-58.3	2.7
O II	3954.36	–	23.4	165.9	16.0	8.74	0.05	–	–
O II	3982.71	3982.12	23.4	100.6	10.0			-44.6	4.0
O II	4069.78	4069.04	25.6	209.7	15.0	8.51	0.02	-54.3	1.3
O II	4072.14	4071.44	25.6	185.7	10.0	8.59	0.02	-51.5	1.3
O II	4132.80	–	25.8	94.0	11.0	8.57	0.05	–	–
O II	4153.29	4152.45	25.8	139.0	10.0			-60.7	1.6
O II	4317.15	4316.39	23.0	160.0	8.0			-53.1	1.3
O II	4319.63	4318.91	23.0	195.8	16.0	8.56	0.01	-50.0	1.0
O II	4345.52	4344.77	23.0	199.0	8.0	8.61	0.02	-51.4	1.0
O II	4347.44	4346.58	25.7	160.0	21.0	8.52	0.01	-59.1	1.3
O II	4349.40	4348.69	23.0	343.0	10.0	8.52	0.01	-48.8	0.6
O II	4351.27	4350.50	25.7	182.5	8.0	8.55	0.02	-53.2	0.9
O II	4366.89	–	28.9	192.3	16.0	8.52	0.03	–	–
O II	4414.90	4414.15	23.4	389.0	31.0			-50.8	0.8
O II	4416.97	4416.23	23.4	319.0	26.0	8.51	0.03	-50.3	1.1
O II	4590.97	4590.12	25.7	193.0	7.0	8.63	0.02	-55.3	0.9
O II	4596.16	4595.28	25.7	155.0	7.0	8.68	0.02	-57.6	1.2
O II	4638.85	4638.05	23.0	236.6	6.0	8.65	0.02	-51.4	0.7
O II	4641.81	4641.03	23.0	312.1	6.0	8.54	0.01	-50.4	0.5
O II	4661.63	4660.85	23.0	236.6	6.0	8.61	0.02	-50.2	0.7
O II	4673.73	–	23.0	46.0	5.0	8.53	0.02	–	–
O II	4676.24	4675.51	23.0	183.6	7.0	8.61	0.02	-46.8	1.0
O II	4699.16	4698.33	28.5	80.7	5.0			-53.0	1.5
O II	4703.16	–	28.5	41.1	8.0	8.52	0.02	–	–
O II	4705.35	–	28.2	125.0	9.0	8.49	0.02	–	–
O II	4710.01	–	26.2	61.9	9.0	8.69	0.03	–	–
O II	4906.83	–	26.3	45.4	8.0	8.49	0.04	–	–
Mg II	4481.23	–	29.6	51.7	7.0	6.56	0.04	–	–
Al III	5696.60	–	15.6	43.8	5.0	5.25	0.05	–	–
Si IV	4116.10	–	24.1	127.5	7.0	7.00	0.04	–	–
Si III	4567.84	–	19.0	288.8	7.0	7.00	0.01	–	–
Si III	4574.76	–	19.0	170.7	7.0	7.14	0.01	–	–
Si III	5739.73	5738.70	19.7	172.0	4.0	7.02	0.01	-54.4	0.8
S III	4253.59	–	18.2	120.3	10.0	6.29	0.03	–	–
S III	4284.97	–	18.2	82.6	13.0	6.33	0.04	–	–
C II	3918.97	–	16.3	119.5	34.0	7.73	0.21	–	–
C III	4647.42	–	29.5	82.3	16.0	7.84	0.19	–	–